Journal of Solid State Chemistry **149,** 391–398 (2000)
doi:10.1006/jssc.1999.8563, available online at http://www.idealibrary.com on IDEAL®

Site Preference of Rare Earth Elements in Hydroxyapatite $[Ca_{10}(PO_4)_6(OH)_2]$

Michael E. Fleet and Xiaoyang Liu

Department of Earth Sciences, University of Western Ontario, London, Ontario N6A 5B7, Canada

and

Yuanming Pan

Department of Geological Sciences, University of Saskatchewan, Saskatoon, Saskatchewan S7N 5E2, Canada

Received July 12, 1999; in revised form October 20, 1999; accepted November 5, 1999

Crystals of rare earth element-(REE)-bearing hydroxyapatites [La–OHAp, Nd–OHAp, Sm–OHAp, Dy–OHAp; $Ca_{10-6x-2y}Na_yREE_{6x+y}(P_{1-x}Si_xO_4)_6(OH)_2$, with $x = 0.036$, $y = 0.045$; space group $P2_1/b$] have been grown from H_2O- and Na-rich phosphate melts and their structures refined in space group $P6_3/m$ at room temperature with single crystal X-ray intensities to $R = 0.019–0.025$. Hydrogen bond valences are in good agreement with a hydrogen-bonded model for the *c*-axis columns of OH^- ions. The crystal/melt partition coefficients for REEs are 3.1, 3.3, 3.0, and 2.4 and REE site occupancy ratios (REE–Ca2/REE–Ca1) are 11, 2.0, 1.6, and 3.3, respectively. The uptake of REEs peaks at Nd, as in REE-substituted fluorapatite (FAp). The REE site occupancy ratio in REE–OHAp and REE–FAp is proportional to the change in unit-cell volume, pointing to some control by spatial accommodation of substituents in the apatite structure. Both the site occupancy ratio and uptake are influenced also by the substitution mechanism, which varies with the volatile anion component. © 2000 Academic Press

INTRODUCTION

Hydroxyapatite [$Ca_{10}(PO_4)_6(OH)_2$; OHAp] is characterized by structural complexity arising from disordering of $(OH)^-$ ions in *c*-axis columns and nonstoichiometry (1, 2). Early research indicated that OHAp has the hexagonal structure of fluorapatite [$Ca_{10}(PO_4)_6F_2$; FAp; space group $P6_3/m$;(3)] but with the OH group displaced from the mirror planes at $z = \frac{1}{4}$ and $\frac{3}{4}$ (4). However, stoichiometric and near-stoichiometric OHAp annealed at high temperature is monoclinic at room temperature with space group $P2_1/b$, $a = 9.4114$ Å, $b \approx 2a$, $c = 6.8814$ Å, and $\gamma \approx 120°$ and has ordered columns of OH^- ions (5, 6). Monoclinic OHAp is further distinguished by very weak reflections that are forbidden by the hexagonal symmetry (6, 7). The transition to hexagonal OHAp occurs at 200–210°C (7). Preservation of the hexagonal $P6_3/m$ space group at room temperature likely results from coherent domains of locally ordered structure generated by impurities and vacancies.

The substitution of rare earth elements (REEs) into apatite results in interesting electron-optical phenomena and is of considerable importance in geochemistry because apatite is usually the dominant host for these trace elements in common rocks. The uptake of trivalent REEs by apatite is not uniform through the 4*f* transition-metal series, but characteristically peaks in the range Nd–Gd for natural apatite and near Nd for synthetic FAp (8), and is lowest for Lu. The overall consistency of this behavior for melts and solvents of widely different composition points to crystal chemical control(s) on REE uptake. The site preference of REEs for the two Ca positions [Ca(1), Ca(2)] in the $P6_3/m$ apatite structure has been investigated using X-ray structures of complex natural (9) and synthetic single crystals (10–14).

In previous studies (12–14) we investigated single-REE-substituted fluorapatite [La–FAp, Nd–FAp, Gd–FAp, Dy–FAp; $Ca_{10-6x-2y}Na_yREE_{6x+y}(P_{1-x}Si_xO_4)_6F_2$, with $x = 0.04–0.05$, $y = 0.3–0.5$; $P6_3/m$], and double-REE-substituted fluorapatite (La,Gd–FAp,Ce,Dy–FAp, Pr,Er–FAp, and Eu,Lu–FAp; with $x = 0.02–03$, $y = 0.3–0.4$; $P6_3/m$). Rare earth elements generally favored the Ca(2) site in FAp (see also (9–11)), but the site occupancy ratios (REE–Ca2/REE–Ca1) decreased monotonically through the 4*f* transition-metal series, rather than peaking at Nd–Gd, and were not quantitatively transferrable to natural apatite. These discrepancies appeared to be related to the accommodation of minor to major amounts of REE in the apatite structure. Although earlier works (13) had pointed

0022-4596/00 $35.00
Copyright © 2000 by Academic Press
All rights of reproduction in any form reserved.

to a correlation between the site preference of REE and the equalization of bond valence, the crystal structures of binary-REE-substituted FAp (14) highlighted the influence of the spatial accommodation and structural change in apatite. In particular, the Ca(1)–O(1), Ca(2)–O(1), P–O(1), and P–O(2), bond distances and the O(1)–P–O(2) bond angle did not vary monotonically through the 4*f* transition-metal series, but had distributions hinged at Nd.

From analysis of mean bond distances and effective ionic radii, it appeared that the volatile anion component (F, OH, Cl) might also be a significant factor in the selectivity of apatite for REE because of its marked influence on the stereochemical environment and effective size of the Ca(2) site (8). It was evident that X-ray structures of REE-substituted OHAp and chlorapatite (ClAp) were required to understand the crystal chemical control(s) on the site preference of REE in apatite because of its chemical and structural complexity.

EXPERIMENTAL PROCEDURES

Single crystals of single-REE-substituted OHAp were grown from volatile-rich melts using a standard cold-seal hydrothermal reaction vessel, closely following procedures for REE-doped FAp (12–14). Calcium REE silicate composition [$Ca_4REE_6(SiO_4)_6O$] was prepared from $CaCO_3$, REE_2O_3, and SiO_2, decarbonated in a platinum dish at 900°C (cf. (15)), and mixed with a commercial synthetic OHAp reagent to give a starting composition containing the equivalent of about 4 mol% $Ca_4REE_6(SiO_4)_6(OH)_2$. Charges consisted of about 0.030 g of the starting composition, 0.030 g of sodium phosphate dodecahydrate ($Na_3PO_4 \cdot 12H_2O$) and 0.01 g of deionized water contained in a sealed gold capsule 2.9 cm in length. They were heated initially to about 920°C at 0.2 GPa, then cooled from 810 to 690°C at 0.01°C/min, maintained at 690°C and 0.12 GPa for 3 days, and quenched in air and water. Crystals of OHAp were analyzed using a JEOL JXA-8600 electron microprobe (EPMA) at the University of Saskatchewan, operated at 5 kV, 10 nA with a beam diameter of 5 μm, and 30-s count times for Ca and P, 60 s for Na and Si, and 90 s for REE. The compositions reported in Table 1 are averages of 10 individual spot analyses.

Single-crystal measurements were made at room temperature and pressure with a Nonius Kappa CCD diffractometer and graphite-monochromatized Mo$K\alpha$ X-radiation (50 kV, 32 mA, $\lambda = 0.70926$ Å). Reflection data were processed with DENZO and SCALEPACK (University of Texas Southwestern Medical Centre at Dallas) and XDISPLAYF (University of Virginia Patent Foundation). SCALEPAC includes an empirical absorption correction based on equivalent reflection intensities. Structure refinements were made with LINEX77 (State University of New York at Buffalo) and closely followed earlier procedures (13, 14). Scattering factors for neutral atomic species and values of f' and f'' were taken, respectively, from Tables 2.2A and 2.3.1 of the "International Tables for X-ray Crystallography" (16). Experimental details are given in Table 2, final parameters in Table 3, and selected bond distances and angles in Table 4.

TABLE 1
Compositions of Synthetic REE-Bearing Hydroxyapatite

Apatite	La–OHAp	Nd–OHAp	Sm–OHAp	Dy–OHAp
P_2O_5(wt%)	39.9(9)	39.1(8)	39.6(6)	40.4(9)
SiO_2	1.3(4)	1.4(3)	1.3(3)	1.0(4)
CaO	52.7(12)	52.2(9)	52.3(8)	53.2(8)
Na_2O	0.12(5)	0.19(7)	0.12(3)	0.11(4)
REE_2O_3	4.5(13)	5.1(11)	4.5(9)	3.8(11)
H_2O[a]	1.73	1.85	1.70	1.73
Total	100.3	99.9	99.5	100.2
	Chemical Formulae Based upon 16 Cations[b]			
P	5.78	5.71	5.78	5.83
Si	0.22	0.24	0.23	0.18
Ca	9.67	9.67	9.68	9.74
Na	0.04	0.06	0.04	0.04
REE	0.29	0.32	0.27	0.21
OH	1.98	2.13	1.96	1.97
O	24.01	23.93	24.02	24.02

[a] H_2O calculated from charge neutrality.
[b] Ideal stoichiometry was assumed for X-ray structure refinement.

TABLE 2
Experimental Details

	La–OHAp	Nd–OHAp	Sm–OHAp	Dy–OHAp
Experiment	AP164	AP165	AP166	AP167
Crystal size ($mm^3 \times 10^3$)	0.21	0.10	0.19	0.45
Crystal shape	prism	prism	prism	prism
a (Å) ($P6_3/m$)	9.4341 (3)	9.4205(8)	9.4202(8)	9.4188(7)
c (Å)	6.8951(3)	6.8846(6)	6.8832(5)	6.8795(4)
Reflections -unique	1174	666	666	1168
-number with ($I < 3\sigma_{(I)}$)	360	231	119	438
Refined parameters	43	43	43	43
μ (cm^{-1})	34.06	36.09	36.10	36.42
R	0.023	0.023	0.019	0.025
R_w	0.024	0.024	0.022	0.026
s	1.207	1.042	1.328	1.033
Extinction ($\times 10^4$)	0.0010(2)	0.0006(2)	0.0010(3)	0.0012(2)
$\Delta\rho$ (e $Å^{-3}$) (+)	0.55	0.48	0.49	0.59
(−)	0.52	0.42	0.47	0.55

TABLE 3
Positional and Isotropic Thermal Parameters (Å²)
($B_{eq} = 4/3 \sum_i \sum_j \beta_{ij}\, a_i \cdot a_j$)

		La–OHAp	Nd–OHAp	Sm–OHAp	Dy–OHAp
Ca(1)	z[a]	0.00127(7)	0.0014(1)	0.00129(7)	0.00130(6)
	B_{eq}	0.94(1)	1.18(3)	1.01(2)	0.96(2)
Ca(2)	x	0.99162(4)	0.99228(7)	0.99248(5)	0.99306(5)
	y	0.24548(4)	0.24599(7)	0.24616(5)	0.24681(5)
	B_{eq}	0.844(7)	0.96(2)	0.77(1)	0.803(8)
P	x	0.36846(5)	0.36836((9)	0.36835(6)	0.36837(6)
	y	0.39826(5)	0.39810(9)	0.39814(6)	0.39804(6)
	B_{eq}	0.639(7)	0.77(1)	0.58(1)	0.646(8)
O(1)	x	0.4845(1)	0.4839(2)	0.4841(2)	0.4839(2)
	y	0.3277(1)	0.3270(2)	0.3271(2)	0.3269(2)
	B_{eq}	1.10(2)	1.15(3)	1.08(2)	1.08(2)
O(2)	x	0.4648(1)	0.4653(2)	0.4652(2)	0.4651(2)
	y	0.5866(1)	0.5866(2)	0.5869(2)	0.5866(2)
	B_{eq}	1.37(2)	1.38(4)	1.29(2)	1.32(2)
O(3)	x	0.2576(1)	0.2576(2)	0.2574(1)	0.2574(1)
	y	0.3427(1)	0.3430(2)	0.3433(2)	0.3431(2)
	z	0.0704(2)	0.0708(2)	0.0704(2)	0.0703(2)
	B_{eq}	1.81(2)	1.89(3)	1.72(2)	1.71(2)
O(H)	z	0.1950(5)	0.1953(7)	0.1951(5)	0.1959(4)
	B_{eq}	1.42(8)	1.35(14)	1.39(10)	1.27(9)
H	z	0.031(14)	0.043(15)	0.061(12)	0.064(9)

[a]Ca(1): $x = \frac{2}{3}$, $y = \frac{1}{3}$: Ca(2), P, O(1), O(2): $z = \frac{1}{4}$. OH: $x = 0$, $y = 0$. H: $x = 0$, $y = 0$, B_{eq} = OH.

RESULTS AND DISCUSSION

The REE-doped OHAp phases presently synthesized were stoichiometric to within the precision of measurement by EPMA; the ratio of total cations in Ca and P positions were 1.667, 1.689, 1.662, and 1.662, for La–, Nd–, Sm–, and Dy–OHAP, respectively (Table 1), and closely comparable to the ideal value of 1.667. Thus, little error was introduced in assuming ideal stoichiometry for the X-ray structure refinements. It is noted that although EPMA probes only to depths of about 1 μm below the surface, the analysis is made on a section through the bulk sample and, with appropriate calibration, is generally quantitative for minerals. Hydrogen is not measured in EPMA and the H_2O contents in Table 1 have been calculated from charge neutrality.

Crystals of REE-doped OHAp were clear and vitreous and of good diffraction quality. Consistent with previous studies on stoichiometric OHAp (5–7), their true symmetry was monoclinic with $b \approx 2a$ and $y \approx 120°$ (space group $P2_1/b$). There was insufficient crystal material for meaningful powder X-ray diffractometry. However, the superstructure reflections characteristic of $P2_1/b$ (6, 7) were well resolved by single-crystal CCD diffractometry. All crystals investigated were mimetic twinned, with twin individuals related by 120° rotation about the c axis (pseudohexagonal axis; (17)). Because of the weak intensity of the monoclinic superstructure reflections (6, 7) and the complex (twinned) reflection intensities, refinement of anisotropic thermal parameters and Ca site occupancies in the monoclinic $P2_1/b$ structure was unsatisfactory. It was also desirable to compare the structures of REE-doped OHAp with those of other apatites refined in $P6_3/m$ (9, 12–14, 18). Therefore, all present structure refinements were made in space group $P6_3/m$.

The O(H) atom was displaced from the horizontal mirror plane as expected (4–6), and the H atom (now with only 50% occupancy) was resolved in all four structure refinements, but was much better in Sm–OHAp and Dy–OHAp than in La–OHAp and Nd–OHAp. The two nearest-neighbor H–O distances for the former two structures (Table 4) correspond to bond valences (and bond valence sums) of 0.884 and 0.096 ($\sum = 0.980$) and 0.906 and 0.096 ($\sum = 1.002$), respectively, which are in excellent agreement with a hydrogen-bonded model for the c-axis columns of OH^- ions (5, 6). The ordered OH^- ions result in alternating direct and hydrogen-bonded linkages [i.e., … H–O(H) … H–O(H) … H–O(H).), where $2[\text{H–O(H)} + \text{H} \ldots \text{O(H)}] = c$. End-member ClAp, like end-member OHAp, is also monoclinic with space group $P2_1/b$ (17), but here the c-axis displacements of Cl accommodate the larger-sized volatile component. It is

TABLE 4
Selected Bond Distances (Å) and Angles (°)

		La–OHAp	Nd–OHAp	Sm–OHAp	Dy–OHAp
Ca(1)–O(1)	×3	2.4098(5)	2.4076(7)	2.4067(6)	2.4066(5)
Ca(1)–O(2)[I]	×3	2.4594(7)	2.459(1)	2.456(1)	2.4565(9)
Ca(1)–O(3)[II]	×3	2.813(1)	2.806(2)	2.803(2)	2.804(1)
mean		2.561	2.557	2.555	2.556
Ca(2)–O(1)[II]		2.694(1)	2.688(2)	2.691(1)	2.692(1)
Ca(2)–O(2)[III]		2.3708(3)	2.3595(6)	2.3593(5)	2.3546(4)
Ca(2)–O(3)	×2	2.5239(6)	2.5141(9)	2.5122(6)	2.5083(6)
Ca(2)–O(3)[IV]	×2	2.345(1)	2.346(2)	2.345(1)	2.343(1)
mean		2.483	2.477	2.477	2.474
Ca2–O(H)		2.3868(6)	2.385(1)	2.3852(8)	2.3872(6)
P–O(1)		1.539(1)	1.537(2)	1.538(2)	1.536(1)
P–O(2)		1.539(1)	1.538(2)	1.540(2)	1.538(1)
P–O(3)	×2	1.5344(9)	1.529(1)	1.532(1)	1.5320(9)
mean		1.537	1.535	1.537	1.535
H–O(H)		1.13(10)	1.05(10)	0.92(9)	0.91(6)
H … O(H)		2.32(10)	2.39(10)	2.52(9)	2.53(6)
O(1)–P–O(2)		111.20(6)	111.22(11)	111.26(9)	111.31(8)
O(1)–P–O(3)[V]	×2	111.29(4)	111.34(7)	111.45(6)	111.39(5)
O(2)–P–O(3)	×2	107.62(5)	107.59(8)	107.44(7)	107.48(6)
O(3)–P–O(3)[V]		107.63(8)	107.57(13)	107.60(10)	107.57(9)

Note. (I) $-x, -y, -z$. (II) $-y, x-y, z$. (III) $y-x, -x, z$. (IV) $x-y, x, -z$. (V) $x, y, \frac{1}{2}-z$.

noted that displacement of the volatile component (X) out of the plane of the ideal $XCa(2)_3$ cluster may be a ubiquitous feature of the apatite structure. For example, in both end-member and REE-doped FAp (10, 19, 12–14) the thermal parameter of F parallel to c is exaggerated ($U_{33} \approx 10 \times U_{11}$) beyond that expected for thermal motion alone.

The uptake of REE by OHAp, as measured by the crystal/liquid partition coefficient (D_{REE}), is about 75% of that for FAp (Table 5), for experiments of similar REE concentrations (8). The substitution of trivalent REE for divlent Ca in FAp crystallized from H_2O-bearing phosphate–fluoride melts was charge compensated by parallel substitution of both Si and Na for P and Ca, respectively, as in the following,

$$REE^{3+} + Si^{4+} = Ca^{2+} + P^{5+},$$

$$Ca_{10-6x}REE_{6x}(P_{1-x}Si_xO_4)_6A_2, \quad [1]$$

$$REE^{3+} + Na^{1+} = 2Ca^{2+},$$

$$Ca_{10-2y}Na_yREE_y(PO_4)_6A_2, \quad [2]$$

(8, 13, 14); these are also the dominant substitution mechanisms for REE-bearing apatite in alkaline igneous rocks (20). In marked contrast, the Na content is subordinate to Si and relatively insignificant in the present OHAp crystals grown from H_2O-bearing Na-rich phosphate melts, whereas Na is dominant to the exclusion of Si in REE-doped ClAp crystals grown from H_2O-bearing Ca-rich, Na-poor phosphate–chloride melts (work in progress).

In refining the present structures of REE-substituted OHAp, Si was assigned a partial occupancy on the P position and Na was restricted to Ca(1). The site occupancy of Na in REE-substituted FAp was refined by iteration (13), resulting in a dominant preference for Ca(1). There was too little Na in the present OHAp crystals for meaningful refinement of its site occupancy and, indeed, the precise occupancy of Na has little bearing on our results. As in previous

TABLE 5
REE Site Occupancies and Site-Occupancy Ratio

	La–OHAp	Nd–OHAp	Sm–OHAp	Dy–OHAp
Ca1 site occupancy Ca	0.986	0.964	0.971	0.982
Na	0.010	0.016	0.010	0.009
REE	0.0043	0.0198	0.0197	0.0090
Ca2 site occupancy Ca	0.955	0.960	0.968	0.971
REE	0.0448(5)	0.0396(8)	0.0320(7)	0.0294(4)
REE–Ca2/REE–Ca1	10.5(22)	2.0(2)	1.63(9)	3.3(3)
Total REE (pfu[a])	0.286	0.316	0.270	0.212
$4f$ electrons per REE^{3+}	0	3	5	9
ΔV^b (Å^3)	+2.75	+0.41	+0.27	−0.17
O(H) bond valence[c] − 1	0.992	0.925	0.916	0.905
$D_{REE:OHAp/melt}$[d]	3.1	3.3	3.0	2.4
	La–FAp	Nd–FAp	Gd–FAp	Dy–FAp
REE–Ca2/REE–Ca1	4.01(22)	2.86(15)	2.00(5)	1.46(4)
Total REE (pfu)	0.650	0.820	0.612	0.518
$4f$ electrons per REE^{3+}	0	3	7	9
ΔV^b (Å^3)	+6.03	+3.59	+1.22	+0.70
F bond valence[c]	0.986	0.967	0.949	0.916
	La,Gd–FAp	Ce,Dy–FAp	Pr,Er–FAp	Eu,Lu–FAp
REE–Ca2/REE–Ca1	2.30(8)	2.29(11)	2.00(8)	1.71(9)
Total REE (pfu)	0.606	0.504	0.474	0.404
$4f$ electrons per REE^{3+}	3.37	3.60	4.35	7.08
ΔV^b (Å^3)	+3.47	+2.82	+1.94	+0.92
F bond valence[c]	0.955	0.927	0.874	0.824

[a] $Ca_{10}(PO_4)_6(OH)_2$.
[b] Deviation from cell volume of end-member OHAp/FAp (2, 19).
[c] After (25).
[d] Partition coefficient.

studies (12–14), only the REE site occupancy of Ca(2), the major carrier of REE, was refined, and other Ca(1) and Ca(2) site occupancies were constrained to the crystal compositions using the following algorithm:

$$\frac{\text{Ca–Ca2}}{2} = 0.5 - \frac{\text{REE–Ca2}}{2}, \quad [3]$$

$$\frac{\text{REE–Ca1}}{3} = \sum \text{REE} - \frac{\text{REE–Ca2}}{2}, \quad [4]$$

$$\frac{\text{Ca–Ca1}}{3} = \sum \text{Ca} - \frac{\text{Ca–Ca2}}{2}, \quad [5]$$

$$\frac{\text{Na–Ca1}}{3} = \sum \text{Na}, \quad [6]$$

where ∑REE, ∑Ca, and ∑Na are the total REE, Ca, and Na cations, respectively, normalized to $(\sum\text{REE} + \sum\text{Ca} + \sum\text{Na}) = \frac{5}{6}$, and Ca–Ca1, Na–Ca1, REE–Ca1, Ca–Ca2, and REE–Ca2 are the site occupancies, whose final values are given in Table 5. The uncertainty in the refined REE site occupancy of Ca(2) due to unsystematic errors is low (1–3%); nevertheless, the error in the REE site occupancy ratio (REE–Ca2/REE–Ca1) becomes large at high values, as $\sigma_{\text{REE–Ca2}}$ approaches the REE site occupancy of Ca(1).

In REE-substituted FAp the REE site occupancy ratio decreased monotonically through the 4*f* transition-metal series from 4.0 in La–FAp to 1.5 in Dy–FAp (8, 12–14; Table 5). These REE-substituted FAp structures were re-refined in this study using the original reflection data because *h*0*l* reflections with $l = 2n + 1$ had been overlooked; however, all positional and thermal parameters, bond distances and angles, and REE site occupancies were identical to those of the previous studies (12–14) within $\pm 1\sigma$. It was also shown earlier (13) that preferential substitution of REE for Ca in Ca(2) leads to equalization of Ca(1) and Ca(2) bond valences and that the F bond valence decreased monotonically through the 4*f* transition-metal series. The FAp crystals investigated in Fleet and Pan (12–14) were not of end-member composition, but varied from 81 to 100% FAp (from 19 to 0% OHAp). Therefore, the F bond valences presently reported for FAp in Table 5 have been recalculated to the actual EPMA compositions. In the present OHAp crystals, La partitions strongly into the Ca(2) position; the REE site occupancy ratio is 11 which is appreciably higher than that of La–FAp (Table 5). The REE site occupancy ratio decreases to 1.6 in Sm–OHAp, lower than that interpolated for Sm–FAp, but then increases to 3.3 in Dy–OHAp. The O(H) bond valence, less 1 unit for H–O(H) and H … O(H) bonds, decreases through the composition series investigated. None of these trends directly accounts for the peak at Nd in the uptake of REE by synthetic FAp and OHAp.

The two Ca positions in the apatite structure offer quite different stereochemical environments (Fig. 1), and this aspect has been focused on in understanding the site preference of substituents (8–10, 12–14, 21, 22). The nearest-neighbor environment of the Ca(1) position (site symmetry 3) is a CaO_9 tricapped trigonal prism, which also can be regarded as a 6 + 3 coordination sphere (12), whereas that of Ca(2) (site symmetry *m*) is a CaO_6X irregular polyhedron. The strong preference of light REE for the Ca(2) position has been variously attributed to a control by substituation mechanism (10), electronegativity difference (21), and equalization of bond valence (9, 12–14). The present observation that the volatile anion component (*X*) exerts a marked control on the substitution mechanism and that the site occupancy ratio for La in OHAp (with negligible Na) is 11 and significantly greater than that for La in FAp (4), (Na ≥ Si) lends support to the conclusion of Mackie and Young (10) who found that minor amounts of Nd substitute for Ca in both Ca(1) and Ca(2) sites in NdF_3-doped FAp but only in Ca(2) in Nd_2O_3-doped FAp. Perhaps charge compensation by Si in OHAp favors REE entering Ca(2) whereas compensation by Na in FAp favors REE entering Ca(1). However, the PO_4 tetrahedron shares two edges with Ca(1) polyhedra, albeit involving the long Ca(1)–O(3) bond distance, and only one with Ca(2), and Na would appear to compensate REE just as readily in a *X*CaNaREE triculster as in adjacent sites of the *c*-axis column of $Ca(1)O_9$ polyhedra. Interestingly, preliminary structure refinement of La–ClAp does indicate a preference of La for Ca(1). Substitution of REE into Ca(2) partially compensates the low bond valence of the volatile anion in FAp and OHAp, and there is a weak correlation between REE site preference and Ca(2)–O(H) bond length in OHAp

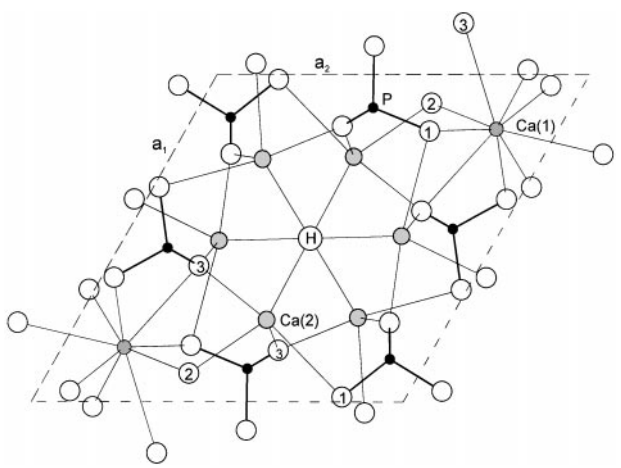

FIG. 1. Structure of hydroxyapatite (OHAp), showing nearest-neighbor environments of Ca(1), Ca(2), P, and O(H).

(Tables 4 and 5). Systematic structure refinements on REE-doped ClAp are required to extend these correlations further.

The effect of spatial accommodation on the uptake of REE by apatite was investigated in Fleet and Pan (8, 14). It was noted that the effective size of the Ca(2) site, which preferentially incorporates light REE in FAp and OHAp, depends on the volatile anion component. By comparing ideal bond distances calculated using effective ionic radii for REE^{3+} and Ca^{2+} (23), it was predicted that Nd would fit most readily in Ca(1) of FAp and OHAp, Nd → Sm most readily in Ca(1) of ClAp, Ce–Pr most readily in Ca2 of FAp and OHAp, and La most readily in Ca(2) of ClAp. Thus, the peaking of observed REE uptake patterns in the range Nd–Gd could be attributed to minimization of local strain. This analysis used structural data for natural FAp, OHAp, and ClAp (18) which, however, were not of end-member composition.

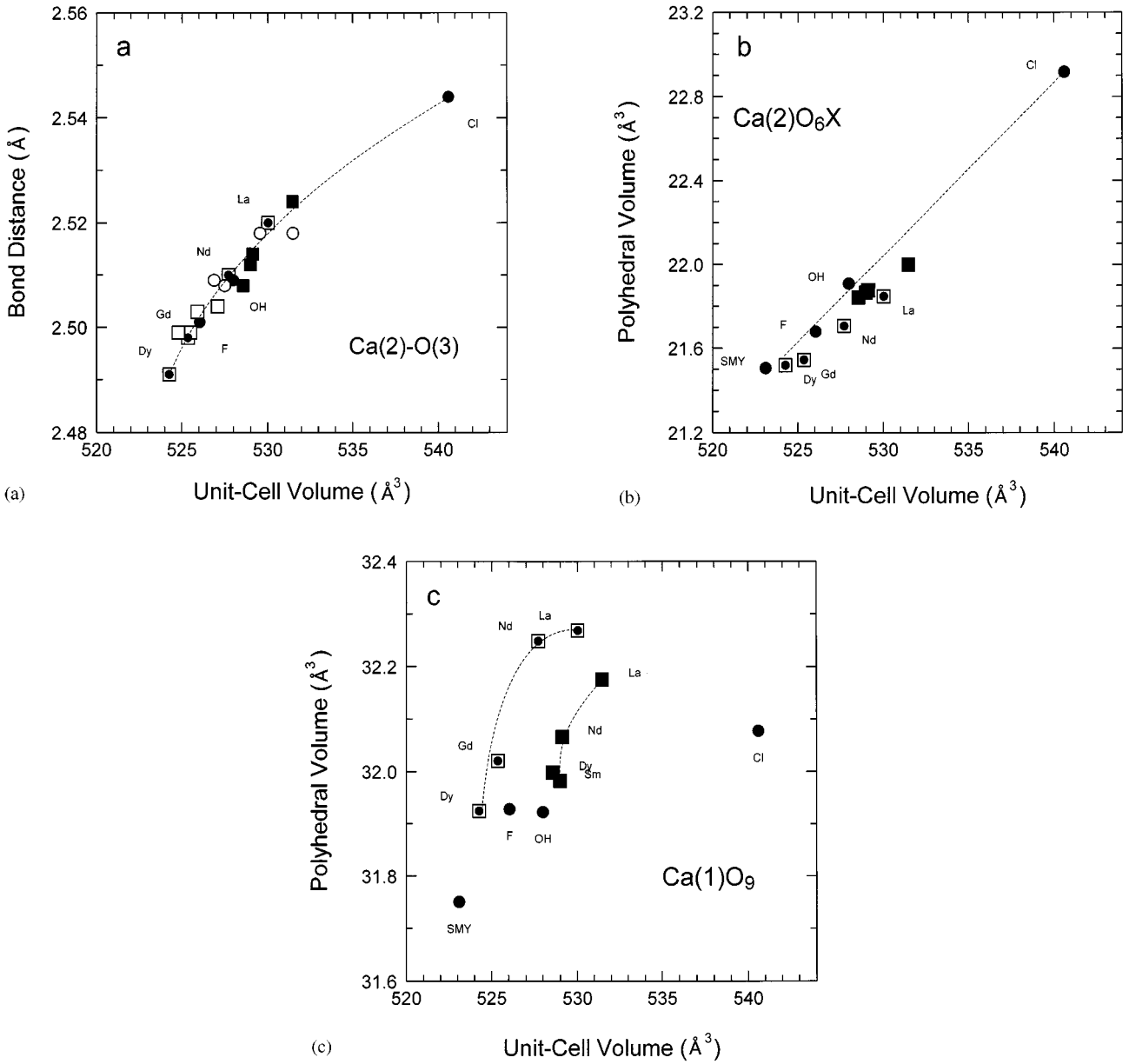

FIG. 2. Variation in (a) Ca(2)–O(3) bond distance, (b) $Ca(2)O_6X$ polyhedral volume, and (c) $Ca(1)O_9$ polyhedral volume with unit-cell volume for REE–OHAp (present study; full squares), single-REE–FAp ((12, 13), open squares with dot), double-REE–FAp ((14), open squares), natural REE–(F, OH)Ap ((9), open circles), and synthetic ((19), SMY), and natural FAp, OHAp, and ClAp ((18), closed circles). Trend lines in Figs. 2 and 3 have been fitted visually.

Investigation of spatial accommodation of REE in apatites is complicated by variation in the quantity of substituents, the differential effects of REE, compensating substituents, and anion components, and the appropriate choice of reference structures. In a comparison of the hexagonal ($P6_3/m$) structures, the substitution of the anion component results in a progressive increase in a and a decrease in c in the sequence FAp → OHAp → ClAp; Ca(2)–O(3), Ca(2)–O(1), and Ca(2)–X increase significantly whereas Ca(2)–O(3)^{IV} (Table 4) and Ca(2)–O(2), decrease; Ca(1)–O(1), increases slightly and Ca(2)–O(2) and Ca(1)–O(3), both decrease. For REE-doped FAp, the distributions of several bond distances and angles hinge at Nd, and there is a weak reversal in trend for Ca(2)–O(H), and some bond distances and angles of the PO_4 tetrahedron between Sm–OHAp and Dy–OHAp (Table 4). All synthetic and natural REE-doped apatites and other natural apatites of hexagonal symmetry exhibit a seemingly continuous variation in size of the Ca(2) polyhedron with substitution, as exhibited by change in both the Ca(2)–O(3) distance and polyhedral volume (Figs. 2a and 2b), where polyhedral volumes have been calculated with VOLCAL (24). In contrast, the polyhedral volume versus the unit-cell volume plot for the Ca(1) position is not consistent with homogeneous change (Fig. 2c), and the separate distributions for the different apatite composition series hinge at Nd and OH; this feature is more evident for the $Ca(1)O_6$ cluster. Although the polyhedral and unit-cell volumes for synthetic end-member FAp (19) are consistent with the data for natural FAp, OHAp, and ClAp (18) and for REE-doped FAp, the Ca(2)–O(3) distance of 2.384 Å is distinctly anomalous compared to Fig. 2a and, if correct, represents an abrupt discontinuity in change of this bond length with progressive substitution toward end-member FAp.

In contradiction of the analysis of ideal bond distances from effective ionic radii (8), substitution of La → Dy in FAp results in an increase in the size of both Ca polyhedra, as does the substitution of La → Sm in OHAp (Figs. 2b and 2c). Volume change is minimized for the REE and apatite combinations investigated only for REE–OHAp between Sm and Dy. These comparisons are made more quantitative by appropriate choice of reference end-member apatite crystal data. Table 5 and Fig. 3 show the difference in unit-cell volumes between REE–OHAp/FAp and end-member hexagonal OHAp (2) and FAp (19); the latter have been corrected linearly for (F, OH)Ap solid solution in the synthetic REE–FAp (12–14).

It is of immediate interest that the plots of the REE site occupancy ratio versus change in the cell volume relative to end-member structures (Fig. 3) converge toward (REE–Ca2/REE–Ca1) = 1 at $\Delta V_{\text{unit cell}} = 0$ (Fig. 3) for both FAp and OHAp. This suggests that minimization of volume strain is an important factor in the dominant preference of REE (and particularly of the larger light REE) for the Ca(2)

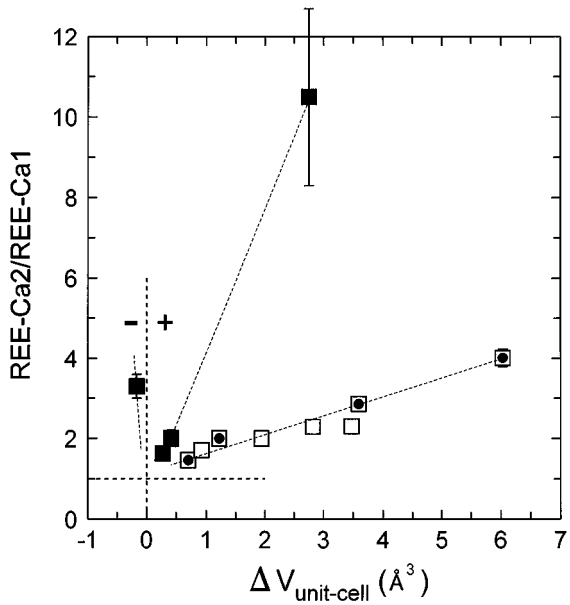

FIG. 3. REE site occupancy ratio (REE–Ca2/REE–Ca1) of REE–OHAp (present study; full squares) and REE–FAp ((12, 13), open squares with dot; (14), open squares) compared with change in unit-cell volume relative to end-member OHAp (2) and (F, OH)Ap solid solution (19, 2), respectively. Note that plots reveal no site preference for REE at $\Delta V_{\text{unit cell}} = 0$.

position. Figure 2b shows that the Ca(2) site readily accommodates substituents. This is a fairly open site, being formed from a hemisphere of 6 oxygens capped by the volatile anion component (Fig. 1). On the other hand, the Ca(2)–O distances and Ca(1) polyhedral volume do not change homogeneously with change in unit-cell volume (Fig. 2c). The $Ca(1)O_6$ polyhedron is a distorted trigonal prism, and we suggest that in FAp and OHAp it does not readily accommodate cations that are either appreciably larger or appreciably smaller than Ca^{2+}. Thus, the REE site occupancy ratio decreases monotonically for FAp through the range of 4f transition-metal series investigated in response to progressive minimization of volume strain. A similar behavior is observed for OHAp, except that somewhere beyond Sm, the REE^{3+} cations become too small for strain-free substitution into Ca(1) and preferentially enter Ca(2). Also, uptake is optimized for $Nd^{3+} \rightarrow Gd^{3+}$ because these cations fit most readily into the Ca positions of FAp and OHAp, although this explanation appears to be more quantitative for OHAp than for FAp.

The REE site occupancy ratio tends to increase asymptotically toward La in both FAp and OHAp, but particularly in the latter. On the basis of volume change, La behaves as though it is appreciably larger than Nd, and other light REEs. This is likely a factor in its strong preference for the Ca(2) position. However, from the rather limited data assembled thus far, there is empirical evidence for

some control by a substitution mechanism on the uptake and site preference of light REE and, in turn, by the volatile anion component on the substitution mechanism. Thus, for phosphate melts, (1) REE substitution into OHAp is charge compensated by Si and results in a strong preference of La for Ca(2) and appreciable REE uptake, which is peaked at Nd with $D_{La} > D_{Dy}$; (2) REE substitution into FAp is charge compensated by both Na and Si (Na > Si) and results in a moderate preference of La for Ca(2) and appreciable REE uptake (FAp > OHAp) peaked at Nd with $D_{La} > D_{Dy} > D_{Lu}$; and (3) REE substitution into ClAp is charge compensated by Na and (provisionally) results in a weak preference of La for Ca(1) and weak REE uptake ($D_{La} < D_{Dy} \approx 0.1$), which is peaked at Sm. This substitution behavior is likely controlled by some complex combination of charge compensation (equalization of bond valence) and spatial accommodation of substituents, although more subtle stereochemical contributions may be significant as well.

ACKNOWLEDGMENTS

We thank Michael Jennings for assistance with collection of X-ray reflection data and the Natural Sciences and Engineering Research Council of Canada for financial support.

REFERENCES

1. J. C. Elliott, "Structure and Chemistry of the Apatites and Other Calcium Orthophosphates." Elsevier, Amsterdam, 1994.
2. J. C. Elliott, *in* "Les matériaux en phosphate de calcium. Aspects fondamentaux" (E. Brès and P. Hardouin, Eds.), p. 25. Sauramps Medical, Montpellier, 1998.
3. A. S. Posner, A. Perloff, and A. F. Diorio, *Acta Crystallogr.* **11,** 308 (1958).
4. M. I. Kay, R. A. Young, and A. S. Posner, *Nature* **204,** 1050 (1964).
5. J. C. Elliott, P. E. Mackie, and R. A. Young, *Science* **180,** 1055 (1973).
6. T. Ikoma, A. Yamazaki, S. Nakamura, and M. Akao, *J. Solid State Chem.* **144,** 272 (1999).
7. H. Suda, M. Yashima, M. Kakihana, and M. Yoshimura, *J. Phys. Chem.* **99,** 6752 (1995).
8. M. E. Fleet and Y. Pan, *Geochim. Cosmochim. Acta* **61,** 4745 (1997).
9. J. M. Hughes, M. Cameron, and A. N. Mariano, *Am. Miner.* **76,** 1165 (1991).
10. P. E. Mackie and R. A. Young, *J. Appl. Crystallogr.* **6,** 26 (1973).
11. R. P. Gunawardane, R. A. Howie, and F. P. Glasser, *Acta Crystallogr. Sect. B* **38,** 1564 (1982).
12. M. E. Fleet and Y. Pan, *J. Solid State Chem.* **111,** 78 (1994).
13. M. E. Fleet and Y. Pan, *Am. Miner.* **80,** 329 (1995).
14. M. E. Fleet and Y. Pan, *Am. Miner.* **82,** 870 (1997).
15. P. J. Wyllie, *J. Am. Ceram. Soc.* **50,** 43 (1967).
16. "International Tables for X-ray Crystallography," (J. A. Ibers and W. C. Hamilton, Eds.), Vol. IV. Kynoch Press, Birmingham, UK, 1974.
17. P. E. Mackie, J. C. Elliott, and R. A. Young, *Acta Crystallogr. Sect. B* **28,** 1840 (1972).
18. J. M. Hughes, M. Cameron, and K. D. Crowley, *Am. Miner.* **74,** 870 (1989).
19. K. Sudarsanan, P. E. Mackie, and R. A. Young, *Mater. Res. Bull.* **7,** 1331 (1972).
20. J. G. Rønsbo, *Am. Miner.* **74,** 896 (1989).
21. V. S. Urusov and V. O. Khudolozhkin, *Geochem. Int.* **11,** 1048 (1974).
22. M. Takahashi, K. Uematsu, Z.-G. Ye, and M. Sato, *J. Solid State Chem.* **139,** 304 (1998).
23. R. D. Shannon, *Acta Crystallogr. Sect. A* **32,** 751 (1976).
24. R. M. Hazen and L. W. Finger, "Comparative Crystal Chemistry." John Wiley, New York, 1982.
25. I. D. Brown, *in* "Structure and Bonding in Crystals," (M. O'Keeffe and A. Navrotsky, Eds.), Vol. II, p. 1. Academic Press, New York, 1981.